Orientation-Matching Minimization for Image Denoising and Inpainting

Jooyoung Hahn · Xue-Cheng Tai · Sofia Borok · Alfred Marcel Bruckstein

Abstract In this paper, we propose an orientation-matching functional minimization for image denoising and image inpainting. Following the two-step TV-Stokes algorithm (Rahman et al. in Scale space and variational methods in computer vision, pp. 473–482, Springer, Heidelberg, 2007; Tai et al. in Image processing based on partial differential equations, pp. 3–22, Springer, Heidelberg, 2006; Bertalmio et al. in Proc. conf. comp. vision pattern rec., pp. 355–362, 2001), a regularized tangential vector field with zero divergence condition is first obtained. Then a novel approach to reconstruct the image is proposed. Instead of finding an image that fits the regularized normal direction from the first step, we propose to minimize an orientation matching cost measuring the alignment between the image gradient and the regularized normal direction. This functional yields a new nonlinear partial differential equation (PDE) for reconstructing denoised and inpainted images. The equation has an adaptive diffusivity depending on the orientation of the regularized normal vector field, providing reconstructed images which have sharp edges and smooth regions. The additive operator splitting (AOS) scheme is used for discretizing Euler-Lagrange equations. We present the results of various numerical experiments that illustrate the improvements obtained with the new functional.

Keywords Orientation-matching minimization ·
TV-Stokes equation · Image denoising · Image inpainting

J. Hahn (✉) · X.-C. Tai · S. Borok · A.M. Bruckstein
Division of Mathematical Sciences, School of Physical and
Mathematical Sciences, Nanyang Technological University,
Singapore, Singapore
e-mail: jyhahn@ntu.edu.sg

X.-C. Tai
e-mail: xctai@ntu.edu.sg

S. Borok
e-mail: sofia.borok@gmail.com

A.M. Bruckstein
e-mail: freddy@cs.technion.ac.il

X.-C. Tai
Mathematics Institute, University of Bergen, Bergen, Norway

A.M. Bruckstein
Department of Computer Science, Technion-Israel Institute of
Technology, Haifa, Israel

1 Introduction

Digital image processing methods based on partial differential equations (PDEs) and variational formulations have been extensively studied for last 20 years both theoretically and in a variety of practical applications. Starting with the Perona-Malik (PM) model in image denoising (Perona and Malik 1990), via directional diffusion methods (Catté et al. 1992), which were preceded by ideas of Gabor (Lindenbaum et al. 1994), and the original Masnou and Morel paper on image inpainting or disocclusion (Masnou and Morel 1998), followed by the work of Bertalmio-Sapiro-Caselles-Ballester (BSCB) model (Bertalmio et al. 2000), hundreds of research papers described various ways to improve the quality of denoising and inpainting. The Rudin-Osher-Fatemi (ROF) model (Rudin et al. 1992) introduced the total variation (TV) based functional to remove noise

while preserving edges and became a fundamental framework in developing variational methods in image processing (Chan and Shen 2005).

Many of the methods for denoising and inpainting images rely heavily on good estimation of image derivatives, and more accurate gradient estimates should lead to better results. Obtaining good estimates of image gradients is a challenging task in image processing because the given image is often degraded or even totally missing over some regions in the image plane. Several researches (Hahn and Lee 2009; Sochen et al. 2004; Perona 1998; Tang et al. 2000; Tschumperlé and Deriche 2002; Chessel et al. 2006; Weickert 1999; Vese and Osher 2002; Spira et al. 2007; Weickert and Welk 2006; Chan et al. 2008) reported impressive results by applying advanced estimation methods for the derivative information. In particular, TV-Stokes (TVS) models regularize the estimation of image gradients and have been successfully applied to image denoising (Rahman et al. 2007) and image inpainting (Tai et al. 2006). The TVS model regularizes the tangential vector field of images by invoking a natural "incompressibility" of flow condition. This constraint guarantees the existence of an image which fits the regularized tangential vector field. Even though the regularized derivatives obtained by the TVS methods are very good, methods of reconstructing images from the regularized vector fields have not been fully explored yet. In this paper, we focus on the reconstruction methods to obtain denoised and inpainted images from the regularized gradient information.

The spatial structures of images are often roughly classified into three categories: flat regions, edges, and ridges or valleys. The flat regions are constant gray-value areas where the level curves of images are not defined. Better denoising and inpainting algorithms recover images preserving more structures. The total variation based functional (Rudin et al. 1992) is very effective for recovering the flat regions and anisotropic diffusion (Weickert 1999) is adjustable to flow-like images. In some sense, these are the second order PDEs for image denoising. It is well known that higher order PDEs (Lysaker et al. 2003) are required to preserve ridges and valleys. In Lysaker and Tai (2006) and Terzopoulos (1988), the authors proposed a smart combination to preserve discontinuities of the image and discontinuities of the gradients of the image surface. We provide more details of the related previous works for image denoising in Sect. 2.1 and image inpainting in Sect. 3.1.

In this paper, inspired by previously introduced two-step algorithms (Rahman et al. 2007; Tai et al. 2006; Bertalmio et al. 2001), we use a regularization of the tangent vector field of an image with zero divergence condition. Then we propose a different approach to reconstruct denoised images and inpainted images from the regularized normal vector field, based on what we call an orientation-matching minimization. We use an orientation matching cost functional measuring the alignment between the image gradient and the regularized normal direction. As opposed to denoising and inpainting models based on the TVS equation (Rahman et al. 2007; Tai et al. 2006), we minimize the direction between the image gradient and the regularized normal direction. The proposed minimization yields a new nonlinear PDE for reconstructing denoised or inpainted images, which exhibits an adaptive diffusivity depending on the orientation of the regularized normal vector field. This provides reconstructed images which have sharp edges and smooth regions.

The paper is organized as follows. In Sects. 2 and 3, we thoroughly review the previous related works and observe some connections between models. Also, we introduce the proposed model for image denoising and image inpainting. Detailed numerical algorithms are explained in Sect. 4. Several numerical examples are presented and different models are compared in Sect. 5. The paper concludes in Sect. 6.

2 Image Denoising

2.1 Review of TV-Stokes Denoising Algorithm

Let us consider a true gray level image $I: \Omega \subset \mathbf{R}^2 \to [0, 1]$. We assume a noisy image I_0 is given as a version of I degraded by additive Gaussian white noise η as follows:

$$I_0(\mathbf{p}) = I(\mathbf{p}) + \eta(\mathbf{p}), \quad \mathbf{p} = (x, y) \in \Omega.$$

The normal and tangential vector fields of the level curves of the image I are

$$\mathbf{n} = \nabla I(\mathbf{p}) = \left(\frac{\partial I}{\partial x}, \frac{\partial I}{\partial y} \right)^{\mathrm{T}} \quad \text{and}$$

$$\mathbf{t} = \nabla^{\perp} I(\mathbf{p}) = \left(\frac{\partial I}{\partial y}, -\frac{\partial I}{\partial x} \right)^{\mathrm{T}}, \tag{2.1}$$

where T denotes a transpose. These vector fields satisfy the condition:

$$\nabla \times \mathbf{n} = 0 \quad \text{and} \quad \nabla \cdot \mathbf{t} = 0, \tag{2.2}$$

hence $\mathbf{n}$ is an irrotational vector field and $\mathbf{t}$ is an incompressible vector field. These properties are crucial when an image must be reconstructed from either $\mathbf{n}$ or $\mathbf{t}$.

The TVS denoising model (Rahman et al. 2007) performs two steps to obtain a denoised image. For the first step, a tangential vector field is regularized with the constraint of incompressibility. The regularized tangential vector field $\mathbf{t}$ is obtained by minimizing the functional:

$$\min_{\nabla \cdot \mathbf{t} = 0} \int_{\Omega} \left(|\nabla \mathbf{t}| + \frac{\delta}{2} |\mathbf{t} - \mathbf{t}_0|^2 \right) d\mathbf{p}, \tag{2.3}$$

where $\mathbf{t}_0 = \nabla^\perp I_0$, δ is a positive parameter, and $|\nabla \mathbf{t}|$ is defined by

$$|\nabla \mathbf{t}| = \sqrt{\left(\frac{\partial u}{\partial x}\right)^2 + \left(\frac{\partial u}{\partial y}\right)^2 + \left(\frac{\partial v}{\partial x}\right)^2 + \left(\frac{\partial v}{\partial y}\right)^2},$$

$$\nabla \mathbf{t} = \begin{pmatrix} \nabla u \\ \nabla v \end{pmatrix}, \quad \mathbf{t} = \begin{pmatrix} u \\ v \end{pmatrix}.$$

The Euler-Lagrange equation and the gradient flow yields the following PDE for regularizing the tangential vector field:

$$
\begin{aligned}
&\frac{\partial \mathbf{t}}{\partial \tau}(\mathbf{p}, \tau) = \nabla \cdot \left(\frac{\nabla \mathbf{t}}{|\nabla \mathbf{t}|}\right) - \delta(\mathbf{t} - \mathbf{t}_0) + \nabla \lambda \quad \text{in} \quad \Omega \times (0, T_1], \\
&\nabla \cdot \mathbf{t} = 0 \quad \text{on} \quad \Omega \times (0, T_1], \\
&\left(\frac{\nabla \mathbf{t}}{|\nabla \mathbf{t}|} + \lambda E\right) \cdot \nu = 0 \quad \text{in} \quad \partial\Omega \times (0, T_1], \\
&\mathbf{t}(\mathbf{p}, 0) = \mathbf{t}_0 \quad \text{in} \quad \Omega,
\end{aligned}
\tag{2.4}
$$

where E is the identity matrix, ν is the outward unit normal vector to the boundary of an image domain $\partial\Omega$, λ is a Lagrange multiplier function to penalize the incompressibility condition. Note that it is not straightforward to apply the PM model (Perona and Malik 1990) or the ROF model (Rudin et al. 1992) directly to regularize derivative information of an image (Hahn and Lee 2009). One of reasons to regularize the tangential vector field is that the incompressibility condition, $\nabla \cdot \mathbf{t} = 0$, is numerically computed using the Chorin projection type method which is well developed in the fluid dynamics; see details in Sect. 4. Moreover, the condition guarantees the existence of an image I such that its normal vector field satisfies the relation (2.2).

Once the regularized tangent vector field $\mathbf{t} = (u, v)^{\mathrm{T}}$ is obtained in the first step, the regularized normal vector field $\mathbf{n}$ is defined by $(v, -u)^{\mathrm{T}}$. Then, the two-step algorithms for image denoising (Lysaker et al. 2004; Rahman et al. 2007) and image inpainting (Tai et al. 2006) suggested to solve the following minimization problem in the second step to reconstruct an image I from $\mathbf{n}$:

$$\min_{\|I - I_0\|_2 = \sigma} \int_\Omega \left(|\nabla I| - \nabla I \cdot \frac{\mathbf{n}}{|\mathbf{n}|}\right) d\mathbf{p},
\tag{2.5}$$

where $\|\cdot\|_2$ is the $L^2(\Omega)$ norm and σ is the standard deviation of a Gaussian white noise. The Euler-Lagrange equation and the gradient flow equation yield the following PDE for recovering the image:

$$
\begin{aligned}
&\frac{\partial I}{\partial \tau}(\mathbf{p}, \tau) = \nabla \cdot \left(\frac{\nabla I}{|\nabla I|} - \frac{\mathbf{n}}{|\mathbf{n}|}\right) - \mu(I - I_0) \\
&\quad \text{on} \quad \Omega \times (0, T_2], \\
&\left(\frac{\nabla I}{|\nabla I|} - \frac{\mathbf{n}}{|\mathbf{n}|}\right) \cdot \nu = 0 \quad \text{in} \quad \partial\Omega \times (0, T_2],
\end{aligned}
\tag{2.6}
$$

$$I(\mathbf{p}, 0) = I_0(\mathbf{p}) \quad \text{in} \quad \Omega,$$

where μ is a positive parameter. If $\frac{\mathbf{n}}{|\mathbf{n}|} = 0$ in the above model, it reduces to the ROF model. Thus, it is natural to expect the TVS model to have a different performance from the TV denoising model; see Fig. 3.

2.2 Orientation-Matching Minimization

In this paper, we use the regularized tangential vector field with zero divergence condition in the first step and propose to combine with a new approach for reconstructing a denoised image in the second step. In contrast to finding an image whose gradient fits the regularized normal direction (2.5), we minimize an orientation matching cost functional measuring the alignment between the image gradient and the regularized normal direction:

$$\min_{\|I - I_0\|_2 = \sigma} \int_\Omega \left(-\frac{|\nabla I \cdot \mathbf{n}|}{|\nabla I||\mathbf{n}|}\right) d\mathbf{p},
\tag{2.7}$$

where $\|\cdot\|_2$ and σ are same as in (2.5). The Euler-Lagrange equation and the gradient flow equation provide here a new PDE for recovering the clean image:

$$
\begin{aligned}
&\frac{\partial I}{\partial \tau}(\mathbf{p}, \tau) = \nabla \cdot \left(\frac{|\nabla I \cdot \mathbf{n}|}{|\nabla I|^2 |\mathbf{n}|} \frac{\nabla I}{|\nabla I|} - \frac{\mathrm{sgn}(\nabla I \cdot \mathbf{n})}{|\nabla I|} \frac{\mathbf{n}}{|\mathbf{n}|}\right) \\
&\qquad\qquad - \mu(I - I_0) \quad \text{on} \quad \Omega \times (0, T_2], \\
&\left(\frac{|\nabla I \cdot \mathbf{n}|}{|\nabla I|^2 |\mathbf{n}|} \frac{\nabla I}{|\nabla I|} - \frac{\mathrm{sgn}(\nabla I \cdot \mathbf{n})}{|\nabla I|} \frac{\mathbf{n}}{|\mathbf{n}|}\right) \cdot \nu = 0 \\
&\quad \text{in} \quad \partial\Omega \times (0, T_2],
\end{aligned}
\tag{2.8}
$$

$$I(\mathbf{p}, 0) = I_0(\mathbf{p}) \quad \text{in} \quad \Omega,$$

where $\mathrm{sgn}(\cdot)$ is the sign function and μ is a positive parameter.

We expect two differences between the previous model (2.5) and the proposed model (2.7). The first is that we have smaller orientation difference between the gradient of an original image and the gradient of a denoised image. The second is that the result in our model will have sharper edges in a denoised image, specially where the original image has smoothly changing pixel values near sharp edges. These phenomena were indeed observed in numerical experiments and there are some plausible reasons for this behavior.

In order to see the first difference, we denote θ as the angle between $\frac{\nabla I}{|\nabla I|}$ and $\frac{\mathbf{n}}{|\mathbf{n}|}$. Then, the functional in the proposed model (2.7) is written as

$$\int_\Omega \left(-\frac{|\nabla I \cdot \mathbf{n}|}{|\nabla I||\mathbf{n}|}\right) d\mathbf{p} = \int_\Omega (-|\cos\theta|) d\mathbf{p}
\tag{2.9}$$

and the functional in the previous model (2.5) is presented by

$$\int_\Omega \left(|\nabla I| - \nabla I \cdot \frac{\mathbf{n}}{|\mathbf{n}|} \right) d\mathbf{p} = \int_\Omega |\nabla I| \left(1 - \frac{\nabla I \cdot \mathbf{n}}{|\nabla I||\mathbf{n}|} \right) d\mathbf{p}$$

$$= \int_\Omega |\nabla I|(1 - \cos\theta)d\mathbf{p}. \quad (2.10)$$

The previous energy functional minimizes both $|\nabla I|$ and the angle θ. If an image I has some regions where $|\nabla I|$ is large enough, the minimization of angle difference between $\frac{\nabla I}{|\nabla I|}$ and $\frac{\mathbf{n}}{|\mathbf{n}|}$ has quite an weak effect. In case of $|\nabla I| \simeq 0$, any angle will fit to $\frac{\mathbf{n}}{|\mathbf{n}|}$. It is clear that the graph of a denoised image is easily deformed to different shapes if the orientation of ∇I is changed very small. Since the proposed energy functional minimizes the orientation difference, a denoised result is more sensitively changed in order to fit the original image. We numerically show the orientation difference in Table 2 using different methods.

The second difference is observed when we assume that ∇I is approximately parallel to $\mathbf{n}$. The proposed PDE can be written by

$$\nabla \cdot \left(\frac{|\nabla I \cdot \mathbf{n}|}{|\nabla I|^2 |\mathbf{n}|} \frac{\nabla I}{|\nabla I|} - \frac{\mathrm{sgn}(\nabla I \cdot \mathbf{n})}{|\nabla I|} \frac{\mathbf{n}}{|\mathbf{n}|} \right)$$

$$\simeq \nabla \cdot \left(\left(\frac{\nabla I}{|\nabla I|} - (\pm) \frac{\mathbf{n}}{|\mathbf{n}|} \right) \frac{1}{|\nabla I|} \right).$$

If $|\nabla I|$ is large, the proposed model (2.8) is dominantly influenced by the data fidelity term and slightly affected by the regularization term. However, the previous model (2.6) is still affected by the additional force term, $\nabla \cdot (\frac{\mathbf{n}}{|\mathbf{n}|})$, from the regularized normal vector field. Since we may have some numerical errors of the vector field, it is difficult to know whether the additional force will generate a good result or not. Even though the extra force reduces the stair-case effect in the TV denoising model on smooth regions, it may derive an erroneous effect near edges where $|\nabla I|$ is large. We numerically show qualities of denoised images when the original image has smoothly changing pixel values near sharp edges; see Figs. 3, 4, and 5.

The functional in the proposed minimization (2.7) is the weighted orientation-matching for each level curve of the image. By using the Coarea formula, the proposed functional is written

$$\int_\mathcal{R} \left(\frac{|\nabla I \cdot \mathbf{n}|}{|\nabla I||\mathbf{n}|} \right) d\mathbf{p}$$

$$= \int_\mathcal{R} \left(\frac{|\nabla I \cdot \mathbf{n}|}{|\nabla I|^2 |\mathbf{n}|} \right) |\nabla I| d\mathbf{p}$$

$$= \int_{-\infty}^\infty \left(\int_{I^{-1}(c)} \frac{1}{|\nabla I(s)|} |\cos(\theta(s))| \, ds \right) dc,$$

where $\theta(s)$ is the angle between the normal vector to the level curve $I^{-1}(c)$ of the image and the regularized normal vector $\mathbf{n}$. In the edge integration context, a similar idea for fitting the angle between the normal vector to level curves of image and the normal vector of the evolving curve was introduced in Kimmel and Bruckstein (2001).

3 Image Inpainting

3.1 Review of TV-Stokes Inpainting Algorithm

Let a gray image be a real-valued function I defined on an open set Ω. We assume that a proper open subset $\mathcal{R}$ of Ω is the region where the image data is missing or corrupted. In Bertalmio et al. (2000), the PDE-based inpainting model was designed by a deep observation of real inpainting work and a transportation phenomenon. It is to obtain a steady state solution of the PDE with the Dirichlet boundary condition on $\partial\mathcal{R}$:

$$\frac{\partial I}{\partial \tau}(\mathbf{p}, \tau) = \nabla (\nabla \cdot \nabla I) \cdot \nabla^\perp I, \quad \text{with} \quad I = I_0 \text{ on } \partial\mathcal{R}. \quad (3.1)$$

The smoothness measure $\nabla \cdot \nabla I$ on the boundary $\partial\mathcal{R}$ is transported along the extended isophotes direction into the inpainting domain. Since it may develop shocks in the domain, an additional diffusion should be used.

In Bertalmio et al. (2001), the authors use an analogy to fluid dynamics in order to extend the smoothness measure along the isophotes direction and the inpainted image is simultaneously reconstructed by the Poisson equation. If we consider an image I as a stream function, the fluid velocity will be $\nabla^\perp I$ and the vorticity ω will be the smoothness measure. Looking at the similarity of the vorticity transport equation in the incompressible Newtonian fluids, the smoothness measure is obtained by a solution of the PDE:

$$\frac{\partial \omega}{\partial t} + \nabla^\perp I \cdot \omega(\omega) = \nu \nabla \cdot (g(|\omega|)\nabla\omega), \quad (3.2)$$

where $g(\cdot)$ makes an anisotropic diffusion with the diffusivity constant ν. Note that $g \equiv 1$ gives the vorticity transport equation in the fluid dynamics. As the vorticity generates the stream function, the inpainted image is simultaneously reconstructed by

$$\nabla \cdot \nabla I = \omega \quad \text{with} \quad I = I_0 \text{ on } \partial\mathcal{R}. \quad (3.3)$$

It smears out edges because the solution should be continuous on Ω.

The strong continuation of the gradient of the image is considered in Ballester et al. (2001) and the inpainted image is simultaneously recovered by an anisotropic diffusion equation based on the following minimization:

$$\min_{\mathbf{n},I} \left(\int_{\mathcal{R}} |\nabla \cdot \mathbf{n}|^p \, (c_1 + c_2 |\nabla k * I|) \, d\mathbf{p} \right.$$

$$\left. + \zeta \int_{\mathcal{R}} (|\nabla I| - \mathbf{n} \cdot \nabla I) \, d\mathbf{p} \right), \tag{3.4}$$

where k denotes a regularizing kernel and the detail admissible sets and other variables are explained in Ballester et al. (2001). Note that the reconstruction which is the second term in the above minimization is very similar to the second step in two-step methods models (Tai et al. 2006; Lysaker et al. 2004; Rahman et al. 2007).

A different approach based on variational formulation, the TV inpainting model, is mathematically studied in Chan and Shen (2002);

$$\frac{\partial I}{\partial \tau}(\mathbf{p}, \tau) = \nabla \cdot \left(\frac{\nabla I}{|\nabla I|} \right), \quad \text{with} \quad I = I_0 \text{ on } \partial \mathcal{R}, \tag{3.5}$$

Even though it has the stair-case effect and a lack of visual connection, it has been a fundamental framework to understand the inpainting process. The curvature-driven diffusion (CCD) model (Chan and Shen 2001) deals with the connectivity principle. Moreover, the authors (Chan et al. 2002) used the strong connection property based on Euler's elastica in Masnou and Morel (1998):

$$\min_I \int_{\mathcal{R}} \phi(\kappa) |\nabla I| \, d\mathbf{p}, \tag{3.6}$$

where $\phi(s) = a + b\kappa^2$ and κ is the curvature of level curves in the image. From the Euler-Lagrange equation and the gradient flow equation, we have:

$$\frac{\partial I}{\partial \tau}(\mathbf{p}, \tau)$$

$$= \nabla \cdot \left(\frac{\phi(\kappa)}{|\nabla I|} \nabla I \right) + \nabla \left(-\frac{\mathcal{D}_{\mathbf{t}} \left(\phi'(\kappa) |\nabla I| \right)}{|\nabla I|^2} \right) \cdot \nabla^{\perp} I,$$

$$\text{with} \quad I = I_0 \text{ on } \partial \mathcal{R}, \tag{3.7}$$

where $\mathcal{D}_{\mathbf{t}}(\cdot)$ is the directional derivative along $\mathbf{t}$. The PDE-based approach to overcome the long connection has been studied in Bertalmio (2006) and Kornprobst and Aubert (2006).

Similar to the TVS denoising model, the TVS inpainting model also consists of two steps. Interestingly, the two-step method in the TVS models can be interpreted by a splitting into the second-order PDEs of the fourth-order PDE in the Lysaker-Lundervold-Tai (LLT) model (Lysaker et al. 2003). The regularization term in the LLT model is

$$\int_{\Omega} \left(\left| \nabla \left(\frac{\partial I}{\partial x} \right) \right|^2 + \left| \nabla \left(\frac{\partial I}{\partial y} \right) \right|^2 \right)^{\frac{1}{2}} d\mathbf{p}. \tag{3.8}$$

Now, the integrand is same as

$$\left| \nabla \left(-\frac{\partial I}{\partial x} \right) \right|^2 + \left| \nabla \left(\frac{\partial I}{\partial y} \right) \right|^2 = |\nabla v|^2 + |\nabla u|^2 = |\nabla \mathbf{t}|^2$$

Instead of solving the fourth-order PDE from the regularization term in the LLT model, the TVS models divide it into two second-order PDEs, the first one is to regularize the tangent vector field with the divergent free condition and the second one is to reconstruct the image with the regularized normal vector field from the first step. This approach has been already introduced in Lysaker et al. (2004) and a different formulation is used to regularize the normal vector field with the constraint of the unit vector. Based on the similar method, the authors in Dong et al. (2009) improved results in image denoising by using the minimization of the angle of the normal vector fields. Recently, some remarkable results in image denoising, specially suitable for recovering sharp vertices and X junctions in the presence of heavy noise, were obtained by estimating double orientations and then reconstructing the image from the estimated information (Steidl 2009).

Now, we briefly review the essential idea of the TVS inpainting. The first step is to obtain construct a regularized tangential vector field $\mathbf{t}$ by minimizing the functional:

$$\min_{\nabla \cdot \mathbf{t} = 0} \int_{\mathcal{R}} |\nabla \mathbf{t}| \, d\mathbf{p}, \quad \text{with} \quad \mathbf{t} = \mathbf{t}_0 \text{ on } \partial \mathcal{R}. \tag{3.9}$$

From the Euler-Lagrange equation and the gradient flow equation, we have the PDE for regularizing the tangential vector field:

$$\frac{\partial \mathbf{t}}{\partial \tau}(\mathbf{p}, \tau) = \nabla \cdot \left(\frac{\nabla \mathbf{t}}{|\nabla \mathbf{t}|} \right) + \nabla \lambda \quad \text{in} \quad \mathcal{R} \times (0, T_1],$$

$$\nabla \cdot \mathbf{t} = 0 \quad \text{on} \quad \mathcal{R} \times (0, T_1], \tag{3.10}$$

$$\mathbf{t}(\mathbf{p}, \tau) = \mathbf{t}_0 \quad \text{in} \quad \partial \mathcal{R} \times [0, T_1],$$

where λ is a Lagrange multiplier function to penalize the incompressibility condition. The total variation norm $|\nabla \mathbf{t}|$ is a reasonable choice because the discontinuity of $\mathbf{t}_0$ on $\partial \mathcal{R}$ should be propagated into the inpainting region $\mathcal{R}$. The incompressibility condition is crucial to guarantee the existence of an image whose normal vector field satisfies the relation (2.1).

In the second step, the inpainted image I is obtained by minimizing the functional with a regularized normal vector field $\mathbf{n} = \mathbf{t}^{\perp}$:

$$\min_I \int_{\mathcal{R}} \left(|\nabla I| - \nabla I \cdot \frac{\mathbf{n}}{|\mathbf{n}|} \right) d\mathbf{p}, \quad \text{with} \quad I = I_0 \text{ on } \partial \mathcal{R}. \tag{3.11}$$

From the Euler-Lagrange equation and the gradient flow equation, we obtain the PDE for reconstructing an image:

$$\frac{\partial I}{\partial \tau}(\mathbf{p}, \tau) = \nabla \cdot \left(\frac{\nabla I}{|\nabla I|} - \frac{\mathbf{n}}{|\mathbf{n}|} \right) \quad \text{on} \quad \mathcal{R} \times (0, T_2],$$

$$I(\mathbf{p}, 0) = I_0(\mathbf{p}) \quad \text{in} \quad \partial \mathcal{R} \times [0, T_2]. \tag{3.12}$$

Unlike reconstructing an image directly from the boundary information of the inpainting region (Bertalmio et al. 2000), the regularized tangential vector field is firstly propagated into the region with the incompressibility condition and then the reconstruction is secondly obtained from the image intensity in $\partial \mathcal{R}$ and the regularized normal vector field on $\mathcal{R}$. The main merit of the TVS inpainting method is that it does not make the stair-case effect on a large inpainting region.

3.2 Orientation-Matching Minimization

It is straightforward to apply a similar idea in Sect. 2.2 to the inpainting problem. However, if we only use the orientation-matching term in the energy functional with the fixed boundary values, it will easily fall into the local minimum and it will be difficult to set the initial condition when we find the minimum from the gradient descent method. As we use the fidelity term for the data in image denoising, we also consider such a fidelity term for the vector data because there is no information of the image data in the inpainting region. Now, we propose the functional to reconstruct an image on the inpainting region from the regularized tangential vector field (3.10):

$$\min_I \left(\bar{\mu} \int_{\mathcal{R}} \left(-\frac{|\nabla I \cdot \mathbf{n}|}{|\nabla I||\mathbf{n}|} \right) d\mathbf{p} + \int_{\mathcal{R}} |\nabla I - \mathbf{n}| d\mathbf{p} \right), \quad \text{with}$$

$$I = I_0 \text{ on } \partial \mathcal{R}, \tag{3.13}$$

where $\bar{\mu}$ is a positive constant and $\mathbf{n} = \mathbf{t}^{\perp}$. The second term is already introduced in Litvinov et al. (2009) and the authors analyze mathematical properties, such as existence and uniqueness of the minimizer. We understand this term as the fidelity for the vector field and it also generates an adaptive regularization effect in the image. The main contribution in this paper is to propose to use the orientation-matching functional in image inpainting and to understand desirable effects from the proposed functional.

From the Euler-Lagrange equation and the gradient flow equation, we obtain a new PDE for reconstructing an image on the inpainting region:

$$\frac{\partial I}{\partial \tau}(\mathbf{p}, \tau) = \bar{\mu} \nabla \cdot \left(\frac{|\nabla I \cdot \mathbf{n}|}{|\nabla I|^2 |\mathbf{n}|} \frac{\nabla I}{|\nabla I|} - \frac{\text{sgn}(\nabla I \cdot \mathbf{n})}{|\nabla I|} \frac{\mathbf{n}}{|\mathbf{n}|} \right)$$

$$+ \nabla \cdot \left(\frac{\nabla I - \mathbf{n}}{|\nabla I - \mathbf{n}|} \right) \quad \text{on} \quad \mathcal{R} \times (0, T_2], \tag{3.14}$$

$$I(\mathbf{p}, \tau) = I_0(\mathbf{p}) \quad \text{in} \quad \partial \mathcal{R} \times [0, T_2].$$

As we have seen some differences between the TVS denoising model and the proposed model in Sect. 2, similar differences between inpainting models (3.11) and (3.13) are observed in numerical experiments.

More interestingly, the PDEs in the TVS inpainting model and the proposed model show additional difference if they are decomposed into a diffusion term and an advection term along the tangent vector field. We decompose the regularized normal vector field into orthogonal directions:

$$\mathbf{n} = \left(\mathbf{n} \cdot \frac{\nabla I}{|\nabla I|} \right) \frac{\nabla I}{|\nabla I|} + \left(\mathbf{n} \cdot \frac{\nabla^{\perp} I}{|\nabla I|} \right) \frac{\nabla^{\perp} I}{|\nabla I|}.$$

Letting θ be the angle between $\frac{\nabla I}{|\nabla I|}$ and $\frac{\mathbf{n}}{|\mathbf{n}|}$, the TVS inpainting model (3.12) can be written as

$$\frac{\partial I}{\partial \tau}(\mathbf{p}, \tau) = \nabla \cdot \left(\frac{\nabla I}{|\nabla I|} - \frac{\mathbf{n}}{|\mathbf{n}|} \right)$$

$$= \nabla \cdot \left(\frac{\nabla I}{|\nabla I|} - \left(\frac{\mathbf{n}}{|\mathbf{n}|} \cdot \frac{\nabla I}{|\nabla I|} \right) \frac{\nabla I}{|\nabla I|} \right.$$

$$\left. - \left(\frac{\mathbf{n}}{|\mathbf{n}|} \cdot \frac{\nabla^{\perp} I}{|\nabla I|} \right) \frac{\nabla^{\perp} I}{|\nabla I|} \right)$$

$$= \nabla \cdot \left(\left(\frac{1 - \cos\theta}{|\nabla I|} \right) \nabla I \right) + \nabla \left(\frac{\sin\theta}{|\nabla I|} \right) \cdot \nabla^{\perp} I.$$

Note that $\frac{\nabla^{\perp} I}{|\nabla I|} \cdot \frac{\mathbf{n}}{|\mathbf{n}|} = -\sin\theta$ and $\nabla I \cdot \nabla^{\perp} I = 0$. The proposed inpainting model (3.14) is written as

$$\frac{\partial I}{\partial \tau}(\mathbf{p}, \tau) = \bar{\mu} \nabla \cdot \left(\frac{|\nabla I \cdot \mathbf{n}|}{|\nabla I|^2 |\mathbf{n}|} \frac{\nabla I}{|\nabla I|} - \frac{\text{sgn}(\nabla I \cdot \mathbf{n})}{|\nabla I|} \frac{\mathbf{n}}{|\mathbf{n}|} \right)$$

$$+ \nabla \cdot \left(\frac{\nabla I - \mathbf{n}}{|\nabla I - \mathbf{n}|} \right)$$

$$= \bar{\mu} \nabla \cdot \left[\left(\frac{|\cos\theta|}{|\nabla I|^2} \right) \nabla I \right.$$

$$- \frac{\text{sgn}(\cos\theta)}{|\nabla I|} \left(\left(\frac{\mathbf{n}}{|\mathbf{n}|} \cdot \frac{\nabla I}{|\nabla I|} \right) \frac{\nabla I}{|\nabla I|} \right.$$

$$\left. \left. + \left(\frac{\mathbf{n}}{|\mathbf{n}|} \cdot \frac{\nabla^{\perp} I}{|\nabla I|} \right) \frac{\nabla^{\perp} I}{|\nabla I|} \right) \right]$$

$$+ \nabla \cdot \left[\left(\frac{1}{|\nabla I - \mathbf{n}|} \right) \nabla I \right.$$

$$- \frac{|\mathbf{n}|}{|\nabla I - \mathbf{n}|} \left(\left(\frac{\mathbf{n}}{|\mathbf{n}|} \cdot \frac{\nabla I}{|\nabla I|} \right) \frac{\nabla I}{|\nabla I|} \right.$$

$$\left. \left. + \left(\frac{\mathbf{n}}{|\mathbf{n}|} \cdot \frac{\nabla^{\perp} I}{|\nabla I|} \right) \frac{\nabla^{\perp} I}{|\nabla I|} \right) \right]$$

$$= \bar{\mu} \nabla \left(\left(\frac{\text{sgn}(\cos\theta)}{|\nabla I|} \right) \frac{\sin\theta}{|\nabla I|} \right) \cdot \nabla^{\perp} I$$

$$+ \nabla \cdot \left(\left(\frac{|\nabla I| - |\mathbf{n}| \cos \theta}{|\nabla I - \mathbf{n}||\nabla I|} \right) \nabla I \right)$$

$$+ \nabla \left(\left(\frac{|\mathbf{n}|}{|\nabla I - \mathbf{n}|} \right) \frac{\sin \theta}{|\nabla I|} \right) \cdot \nabla^\perp I.$$

Comparing with the TVS inpainting models in Tai et al. (2006) and Litvinov et al. (2009), the proposed orientation-matching functional yields additional transportation effect. It explains that the proposed model (3.13) have better connectivity property then the TVS inpainting models from the same regularized normal vector field in the first step. It is numerically observed in Fig. 8.

We see that the TVS inpainting model and the proposed inpainting model have an adaptive diffusivity depending on the angle θ and an adaptive transportation effect. When the angle $\theta = \pi$, it means that the gradient of image is exactly opposite direction to the regularized normal vector. A strong diffusion along the direction fill in the image data from the boundary into the inpainting regions. Moreover, when the angle $\theta = \pm \frac{\pi}{2}$, the diffusion does not happen and the smoothness measures are transported into the inpainting regions along the isophotes direction. The adaptive advection reduces the shock effect in the inpainting region because $\theta = \pi$ or 0 makes the smoothness measure zero. We draw an attention that the TVS inpainting method and the proposed model consists of the adaptive diffusivity and the transportation phenomenon in PDEs (3.12) and (3.14). Note that we do not discretize the decomposed equations to compute the reconstructed images.

Comparing with the diffusivity depending on the curvature of the level curves in Chan and Shen (2001) and Bertalmio (2006), the TVS inpainting model and the proposed inpainting model seems to be troubled with the connectivity principle (Chan and Shen 2001). However, the connectivity is easily achieved as long as the regularized normal vector field is well obtained in the first step. Even though the obtained vector field is smooth across the edges, we numerically observe the connectivity property if $\bar{\mu}$ is large; see Fig. 8.

4 Numerical Aspects

We use the standard staggered grid suggested in Tai et al. (2006) and Rahman et al. (2007). An example of grid system for discretizing PDEs (3.10), (3.12), and (3.14) in image inpainting is shown in Fig. 1. The red region is a given inpainting domain. All black nodes are computational nodes and all blue nodes are boundary nodes. In the regularization step for the tangent vector field, u and v in (4.1) are defined at $\square$ nodes and $\circ$ nodes, respectively, and λ in (4.2) is defined at $\triangle$ nodes. In the reconstruction step, the image intensity I is defined at $\bullet$ nodes. We also use a similar grid
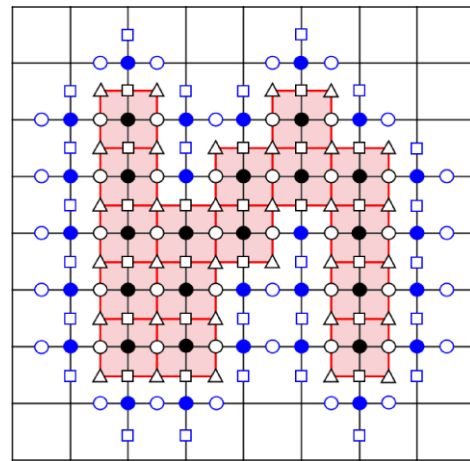

Fig. 1 (Color online) A grid system for discretizing PDEs of image inpainting: The *red region* is an inpainting region. All *black nodes* are computational nodes and all *blue nodes* are boundary points. u and v in (4.1) are defined at points marked by $\square$ and $\circ$, respectively. λ in (4.2) is defined at points marked by $\triangle$. The image intensity I is defined at points marked by $\bullet$

system for discretizing PDEs (2.4), (2.6), and (2.8) in image denoising with a rectangular red region which is the domain of the image. In this section, some issues of discretization are discussed in image denoising. In the case of image inpainting, we briefly comment what should be changed.

4.1 A Regularization of the Tangent Vector Field

The minimization problem (2.3) for regularizing the tangent vector field with the constraint of the incompressibility condition is solved by the method of Lagrange and the Chorin projection type method. We apply the Chorin projection type method and the AOS method (Lu et al. 1992) to solve the PDE (2.4). The algorithm we present below is essentially the same algorithm as the one used in Lu et al. (1992) for Navier-Stokes equations.

1. Calculation for the intermediate tangent field $\mathbf{t}^*$ which is not incompressible vector field:

$$\frac{\mathbf{t}^* - \mathbf{t}^n}{\Delta \tau} = \nabla \cdot \left(\frac{\nabla \mathbf{t}^*}{|\nabla \mathbf{t}^n|_\epsilon} \right) - \delta(\mathbf{t}^* - \mathbf{t}_0), \qquad (4.1)$$

with the boundary condition

$$\nabla \mathbf{t}^* \cdot v = 0,$$

where $|\nabla \mathbf{t}^n|_\epsilon \equiv \sqrt{\epsilon + |\nabla \mathbf{t}^n|^2}$ and $\mathbf{t}^n$ is the tangent vector field at the nth time step. The AOS method (Lu et al. 1992; Weickert et al. 2001) of the linearized equation for the component u is

$$\frac{u^{n+\frac{1}{2}} - u^n}{2\Delta \tau} = \frac{\partial}{\partial x} \left(\frac{1}{|\nabla \mathbf{t}^n|_\epsilon} \left(\frac{\partial u}{\partial x} \right)^{n+\frac{1}{2}} \right)$$

$$- \frac{\delta}{2} \left(u^{n+\frac{1}{2}} - u_0 \right),$$

$$\frac{\tilde{u}^{n+\frac{1}{2}} - u^n}{2\Delta\tau} = \frac{\partial}{\partial y} \left(\frac{1}{|\nabla \mathbf{t}^n|_\epsilon} \left(\frac{\partial \tilde{u}}{\partial y} \right)^{n+\frac{1}{2}} \right)$$

$$- \frac{\delta}{2} \left(\tilde{u}^{n+\frac{1}{2}} - u_0 \right),$$

$$u^* = \frac{1}{2} \left(u^{n+\frac{1}{2}} + \tilde{u}^{n+\frac{1}{2}} \right).$$

The first and second equations yield tridiagonal systems of equations for $u^{n+\frac{1}{2}}$ and $\tilde{u}^{n+\frac{1}{2}}$, respectively. The spatial derivatives with respect to x and y are approximated by the standard one-sided finite differences. Similar equations hold for the component v. More details are shown in Tai et al. (2006) and Rahman et al. (2007). In the case of image inpainting, $\delta = 0$ and the Dirichlet boundary condition are used. Since the computational domain is irregular, the splitting into x and y directions in the AOS method (Lu et al. 1992; Weickert et al. 2001) should be carefully done. It is basically a line by line selection to apply the method in the irregular domain. For instance, we need to solve 11 systems of equations along the x-direction and 5 systems of equations along the y-direction for updating u^* defined at points marked by black □ in Fig. 1. The boundary values on each line are obtained by ends of the line.

2. Solving for λ such that

$$\begin{cases} \dfrac{\mathbf{t}^{n+1} - \mathbf{t}^*}{\Delta\tau} = \nabla\lambda, \\ \nabla \cdot \mathbf{t}^{n+1} = 0. \end{cases}$$

This gives the Poisson equation for λ with zero Neumann boundary condition; see Lu et al. (1992):

$$\nabla \cdot \nabla\lambda = -\frac{1}{\Delta\tau} \nabla \cdot \mathbf{t}^*. \qquad (4.2)$$

λ is approximated at nodes marked by △ in Fig. 1 and the right hand side of the above equation at same nodes is easily discretized because the ends of five stencil at the mark △ are the marks □ and ○ for approximating u and v, respectively. In the case of image inpainting, we use the standard finite element method to deal with irregular inpainting domains and the Neumann boundary condition.

3. Updating the tangent vector field by

$$\mathbf{t}^{n+1} = \mathbf{t}^* + \Delta\tau \nabla\lambda.$$

For the stopping criterion, we use the steady state condition for the flow $\mathbf{t} = (u, v)^{\mathrm{T}}$:

$$\max \left(\frac{\|u^{n+1} - u^n\|_\infty}{\|u^n\|_\infty}, \frac{\|v^{n+1} - v^n\|_\infty}{\|v^n\|_\infty} \right) \leq \alpha,$$

where n and $n+1$ are consecutive time steps and $\|\cdot\|_\infty$ is the $L^\infty(\Omega)$ norm. Note that $\alpha = 10^{-4}$ and $\alpha = 10^{-5}$ are fixed for image denoising and image inpainting, respectively.

4.2 A Reconstruction of an Image

After the regularized tangent vector field $\mathbf{t} = (u, v)^{\mathrm{T}}$ is computed from the first step, we propose the orientation-matching minimization (2.7) and (3.13) to reconstruct a denoised image and an inpainted image, respectively, from the regularized normal vector field $\mathbf{n} = (-v, u)^{\mathrm{T}}$. The Euler-Lagrange equation and the gradient descent flow yields new PDEs (2.8) and (3.14). We also apply the AOS method to solve the PDE (2.8) for image denoising:

$$\frac{I^{n+\frac{1}{2}} - I^n}{2\Delta\tau} = \frac{\partial}{\partial x} \left(A^n \left(\frac{\partial I}{\partial x} \right)^{n+\frac{1}{2}} \right) - \frac{\mu}{2} I^{n+\frac{1}{2}} + \frac{F^n}{2},$$

$$\frac{\tilde{I}^{n+\frac{1}{2}} - I^n}{2\Delta\tau} = \frac{\partial}{\partial y} \left(A^n \left(\frac{\partial \tilde{I}}{\partial y} \right)^{n+\frac{1}{2}} \right) - \frac{\mu}{2} \tilde{I}^{n+\frac{1}{2}} + \frac{F^n}{2}, \quad (4.3)$$

$$I^{n+1} = \frac{1}{2} \left(I^{n+\frac{1}{2}} + \tilde{I}^{n+\frac{1}{2}} \right),$$

where

$$A^n = \frac{|\nabla I^n \cdot \mathbf{n}| + \epsilon}{|\nabla I^n|_\epsilon^3 |\mathbf{n}|_\epsilon},$$

$$F^n = -\nabla \cdot \left(\frac{\mathrm{sgn}_\varepsilon(\nabla I^n \cdot \mathbf{n})}{|\nabla I^n|_\epsilon} \frac{\mathbf{n}}{|\mathbf{n}|_\epsilon} \right) + \mu I_0. \qquad (4.4)$$

The first and second equations (4.3) give tridiagonal systems of equations for $I^{n+\frac{1}{2}}$ and $\tilde{I}^{n+\frac{1}{2}}$, respectively. The spatial derivatives with respect to x and y are approximated by the standard one-sided finite differences. More details are shown in Rahman et al. (2007) and Tai et al. (2006). The initial condition $I(\mathbf{p}, 0)$ is the noisy image.

In the case of image inpainting, $\mu = 0$ is used in the above equations and the diffusivity and the force term in (4.3) is changed for discretizing the proposed PDE (3.14):

$$A^n = \bar{\mu} \frac{|\nabla I^n \cdot \mathbf{n}| + \epsilon}{|\nabla I^n|_\epsilon^3 |\mathbf{n}|_\epsilon} + \frac{1}{|\nabla I^n - \mathbf{n}|_\epsilon},$$

$$F^n = -\bar{\mu} \nabla \cdot \left(\frac{\mathrm{sgn}_\varepsilon(\nabla I^n \cdot \mathbf{n})}{|\nabla I^n|_\epsilon} \frac{\mathbf{n}}{|\mathbf{n}|_\epsilon} \right) - \nabla \cdot \left(\frac{\mathbf{n}}{|\nabla I^n - \mathbf{n}|_\epsilon} \right). \qquad (4.5)$$

The Dirichlet boundary condition is used. Since the computational domain is irregular, the splitting into x and y directions in the AOS method (Lu et al. 1992; Weickert et al. 2001) should be carefully done. It is basically a line by line selection to apply the method in the irregular domain. For instance, we need to solve 10 systems of equations along the x-direction and 5 systems of equations along the y-direction

for updating I^{n+1} defined at points marked by black • in Fig. 1. The boundary values on each line are obtained on ends of the line. The initial condition $I(\mathbf{p}, 0)$ is zero in the inpainting domain.

A parameter ϵ is used to avoid division by zero in numerical experiments:

$$|\nabla I^n|_\epsilon \equiv \sqrt{\epsilon + |\nabla I^n|^2}, \quad |n|_\epsilon \equiv \sqrt{\epsilon + |n|^2}.$$

The ϵ in the numerator of A^n in (4.4) and (4.5) is necessary in order to prevent an infinitesimal diffusivity. Note that $\text{sgn}_\varepsilon(\cdot)$ is a smeared sign function (Chan and Vese 2001).

$$\text{sgn}_\varepsilon(s) \equiv 2H_\varepsilon(s) - 1,$$

$$H_\varepsilon(s) \equiv \begin{cases} 1 & s > \varepsilon, \\ 0 & s < \varepsilon, \\ \frac{1}{2}\left(1 + \frac{s}{\varepsilon} + \frac{1}{\pi}\sin\left(\frac{\pi s}{\varepsilon}\right)\right) & \text{otherwise,} \end{cases}$$ (4.6)

we use $\varepsilon = 1$ for examples in image denoising and we use small ε in image inpainting. Specific values are shown in each example. The parameter should not be too small because the positive ε makes adaptive diffusion effect in image denoising. Considering the decomposition of the regularized normal vector field $\mathbf{n}$ of F^n in (4.4) along $\frac{\nabla I^n}{|\nabla I^n|}$ and $\frac{\nabla^\perp I^n}{|\nabla I^n|}$, $\text{sgn}_\varepsilon(\cdot)$ is related to the diffusivity in the previous time step. The reason we obtain sharp edges in the presence of such a relative large ε is that the diffusivity is changed adaptively depending on the regularized normal vector field. Unfortunately, it is no longer to solve the approximate solution which satisfies (2.7) when $\varepsilon > 0$. The numerical method to solve the proposed PDE in image denoising should be studied further to obtain more exact results. In case of image inpainting, the parameter ε can be a small value because (3.14) has the regularization term of the image which can be interpreted as the fidelity term for the vector data.

For the stopping criterion in image denoising, we use the steady state condition for the relative difference in the energy (2.7). That is,

$$\frac{|E^{n+1} - E^n|}{|E^n|} \leq \beta,$$

where E^n is the energy value at the time step n approximated by

$$E^n \approx \sum_{i,j}\left(-\frac{|\nabla I^n \cdot \mathbf{n}|}{|\nabla I^n|_\epsilon |\mathbf{n}|_\epsilon}\right).$$

The value of β may be different for images and we use $10^{-2} \leq \beta \leq 10^{-4}$. The energy (2.5) is similarly computed and it is used for the stopping criterion of the second step in the previous model (2.6). For the stopping criterion in image
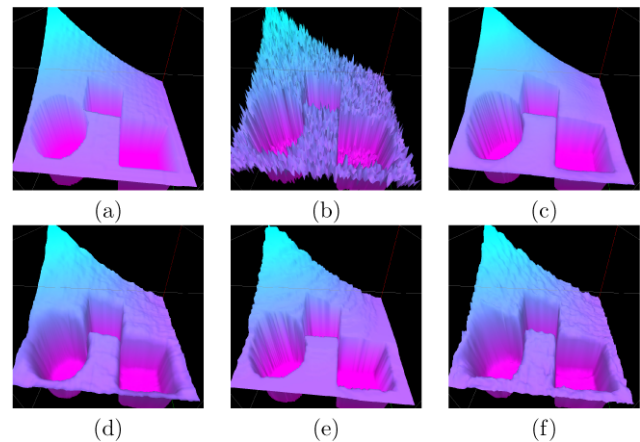

(a) (b) (c)

(d) (e) (f)

Fig. 3 Comparison with other methods in image denoising: (**a**), (**b**), and (**c**) are the graph of images from top to bottom of the test 5 in Fig. 2, respectively. (**d**) is the result of the TVS denoising model and (**e**) is the result of the TV denoising model. (**f**) is the result from (5.1). Note that (**c**) is the result from the proposed model

inpainting, we use the steady state condition for the energy. That is, we stop the numerical computation for reconstructing images when the graph of energy in Fig. 9 is almost horizontal.

The right choice of parameters is crucial for qualities of reconstructing images. The parameters, δ and μ, controls the balance between data smoothing and the fidelity term. The parameter ϵ is used to avoid a division by zero, which also influences the diffusivity for smoothing a data. The AOS scheme provides us a wide range of the time step. However, if $\Delta\tau$ is too large, then visual qualities of a denoised image are deteriorated.

5 Examples

In this section, we show numerical experiments for denoising and inpainting images based on the proposed methods. With synthetic images and real images, we discuss the strength of the proposed orientation-matching minimization and compare with results from other methods. For simplicity, the notations in Table 1 are used to indicate parameters in different methods. For the TV inpainting model, $\Delta\tau$ is the time step and ϵ indicates the same regularization parameter to prevent from dividing zero when we discretize (3.5) in the standard method.

Information of orientation of the gradient of images has also been used in for image restoration (Brox et al. 2006; Weickert 1999; Spira et al. 2007; Weickert and Welk 2006; Chan et al. 2008). Here we use the regularized vector $\mathbf{n}$ to obtain the orientation of the gradient and put this into the PDE-based model (Brox et al. 2006; Weickert 1999) for image denoising and image inpainting. The diffusivity tensor

Table 1 Some notations to indicate different parameters in PDEs for image denoising and image inpainting

	Parameters in image denoising	Parameters in image inpainting
	$V(\Delta\tau, \delta, \epsilon)$: (2.4)	$V(\Delta\tau, \epsilon)$: (3.10)
	$M^1(\Delta\tau, \mu, \epsilon)$: (2.8)	$M^1(\Delta\tau, \bar{\mu}, \epsilon, \varepsilon)$: (3.14)
	$M^2(\Delta\tau, \mu, \epsilon)$: (2.6)	$M^2(\Delta\tau, \epsilon)$: (3.12)
	$M^3(\lambda)$: the TV denoising method in Bresson and Chan (2008)	$M^3(\Delta\tau, \epsilon)$: the TV inpaiting method
	$M^4(\mu, \rho, \epsilon)$: (5.1)	$M^4(\Delta\tau, \rho, \epsilon)$: (5.1)

Fig. 2 Results from the proposed method: the *first row* is original images, we add a Gaussian white noise with zero mean and the standard deviation 10 for all images in the *second row*, and the *last row* is the result from the proposed method

(test 1) (test 2) (test 3) (test 4) (test 5)
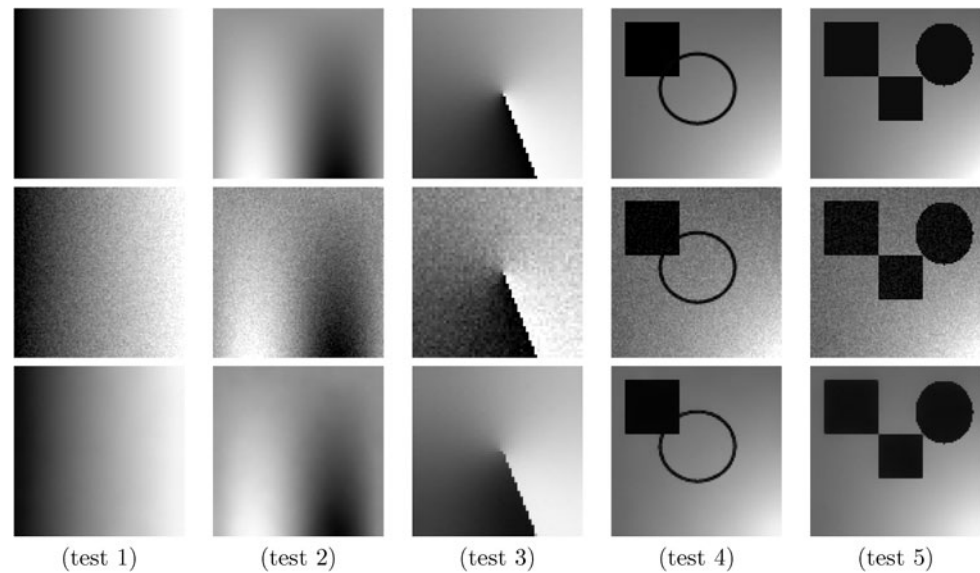
Table 2 Comparison of the orientation difference γ in (5.2): (A) is the result of the proposed method, (B) is the result of the TVS denoising method, (C) is the result of the TV-filter method. The denoised image from the prosed method is shown in the third row of Fig. 2
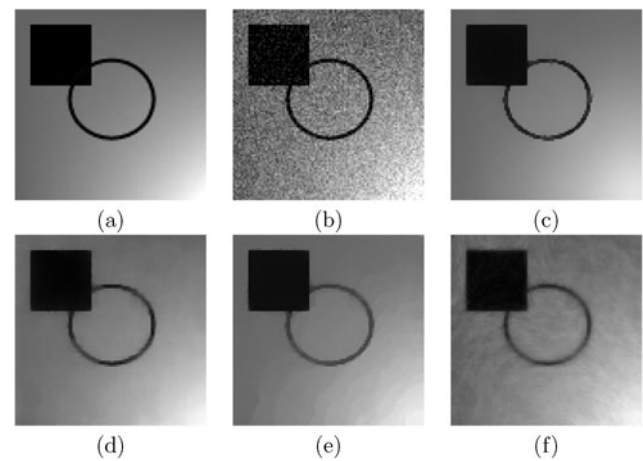
Images	Test 1	Test 2	Test 3	Test 4	Test 5
(A)	0.9706	0.8693	0.7668	0.5681	0.4936
(B)	0.9316	0.8478	0.6304	0.4983	0.4051
(C)	0.7466	0.6825	0.6218	0.3891	0.3228

(a) (b) (c)

(d) (e) (f)

Fig. 4 (**a**) is an original image. We add a Gaussian white noise with zero mean and the standard deviation 20 in (**b**) which is larger noise than in test 4 in Fig. 2. (**c**) is the result of the proposed model. (**d**) is the result of the TVS denoising model and (**e**) is the result of the TV denoising model. (**f**) is the result from (5.1)

is constructed from $\mathbf{n} = (-v, u)^{\mathrm{T}}$ and we solve the following PDE with the free flux boundary condition to obtain a denoised image:

$$\frac{\partial I}{\partial \tau}(\mathbf{p}, \tau) = \nabla \cdot \left(g\left(G_\rho * \mathbf{n}\mathbf{n}^{\mathrm{T}}\right)\nabla I\right) - \mu(I - I_0), \qquad (5.1)$$

where $(G_\rho * M)_{ij} = G_\rho * m_{ij}$ for a matrix $M = (m_{ij})$ and $G_\rho * f$ is the convolution of f with the two-dimensional Gaussian kernel with the standard deviation ρ. The function g is defined on a set $\mathcal{S}$ of real semi-positive symmetric 2×2 matrices:

$$g(M) \equiv \frac{1}{\sqrt{\epsilon + \Lambda_1}} v_{\Lambda_1} v_{\Lambda_1}{}^{\mathrm{T}} + \frac{1}{\sqrt{\epsilon + \Lambda_2}} v_{\Lambda_2} v_{\Lambda_2}{}^{\mathrm{T}},$$

where $(\Lambda_1, v_{\Lambda_1})$ and $(\Lambda_2, v_{\Lambda_2})$ are eigenpairs of $M \in \mathcal{S}$, $\Lambda_1 \geq \Lambda_2$. In the case of image inpainting, $\mu = 0$ and the Dirichlet boundary condition is used. The same type of grid system in Fig. 1 is applied to discretize the PDE (5.1) and we use the standard explicit method for discretizing the time.

Fig. 5 (**a**) is a part of a tangent vector field from (2.3). (**a1**), (**a2**), and (**a3**) in the *first row* are a part of the images (**c**), (**d**), (**f**) in Fig. 4, respectively. In the *second row*, we compute less smooth tangent vector field (**b**) in the first step and use the same method for the second step as the *first row*
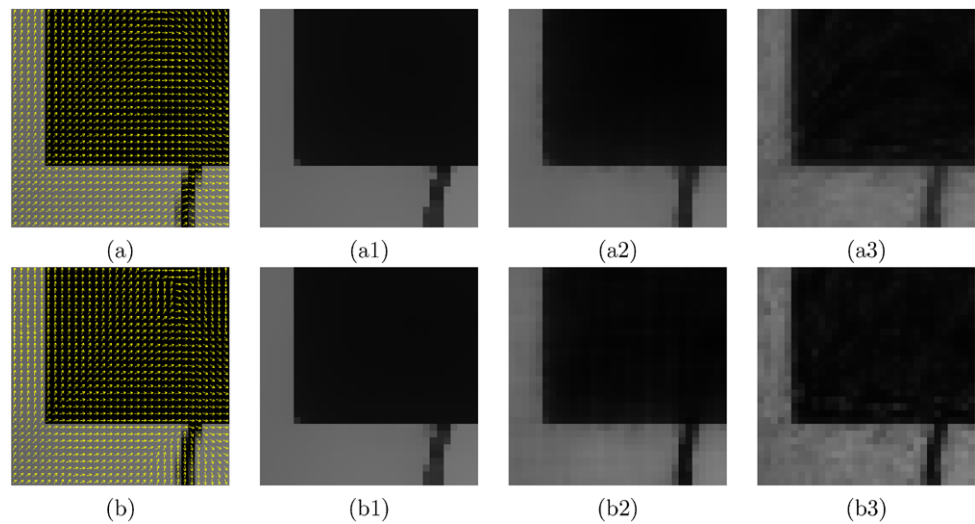
Fig. 6 There is a Gaussian white noise with zero mean and the standard deviation 10 in (**a**) from Martin et al. (2001). (**b**) is the result from the proposed model. (**c**) is the result of the TVS denoising model and (**d**) is the result of the TV denoising model. The size of image is 240×124
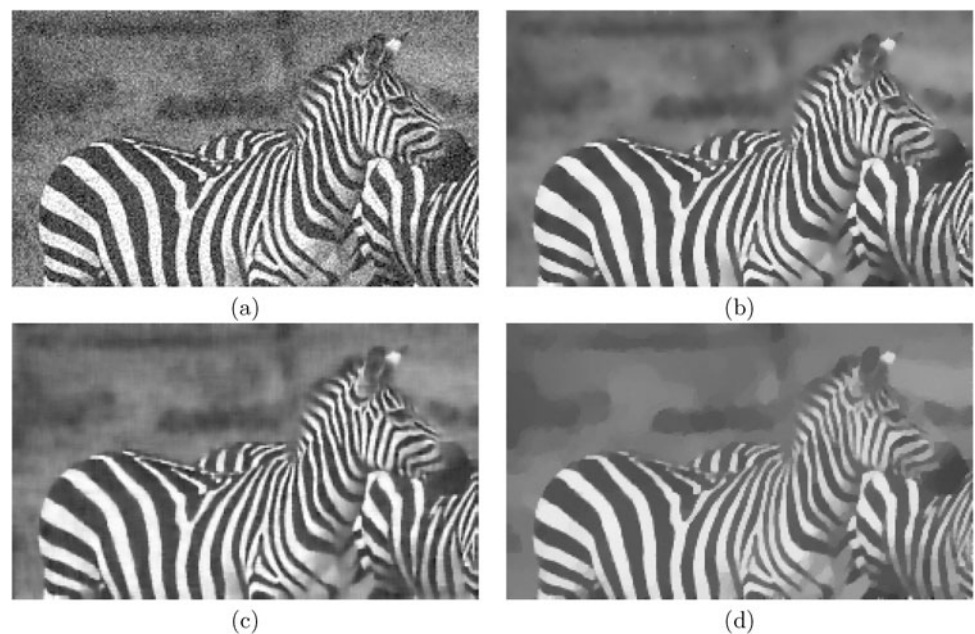
Table 3 Comparison of the orientation difference γ (5.2) for images in Fig. 8

| Images in Fig. 8	(b1)	(b2)	(b3)	(b4)
The first row	0.7018	0.6675	0.6495	0.5977
The third row	0.9155	0.9152	0.9103	0.8856

Example 1

We numerically check how well the orientation of the gradient of a denoised image is fitted to the gradient of the original image. In Table 2, we measure the orientation difference

for different test images:

$$\gamma = \frac{1}{|\Omega|} \int_{\Omega} \left| \frac{\nabla I_e}{|\nabla I_e|} \cdot \frac{\nabla I_c}{|\nabla I_c|} \right| d\mathbf{p}, \qquad (5.2)$$

where I_e is the original image, I_c is the computed denoised image, and $|\Omega|$ is the area of the domain. In the first step in (A) and (B), $V(0.1, 1, 10^4)$ is fixed for all test images. In the second step in (A) and (B), $M^1(10^{-3}, 1, 10^{-3})$ and $M^2(10^{-3}, 1, 10^{-6})$ for test 1, $M^1(10^{-3}, 1, 5 \cdot 10^{-3})$ and $M^2(10^{-3}, 1, 2.5 \cdot 10^{-5})$ for test 2, $M^1(10^{-3}, 1, 2.5 \cdot 10^{-5})$ and $M^2(10^3, 1, 5 \cdot 10^{-3})$ for test 3, $M^1(10^{-3}, 1, 10^{-3})$ and $M^2(10^{-3}, 5, 10^{-3})$ for test 4, and $M^1(10^{-3}, 2, 3 \cdot 10^{-3})$ and $M^2(10^{-3}, 3, 3 \cdot 10^{-3})$ for test 5 are used, respectively. In (C), all results are obtained by $M^3(60)$. As we explain in Sect. 2.2, the proposed model has better performance for fit-

Fig. 7 There is a Gaussian white noise with zero mean and the standard deviation 10 in (**a**) from Martin et al. (2001). (**b**) is the result of the proposed model. (**c**) is the result of the TVS denoising model and (**d**) is the result of the TV denoising model. The size of image is 181×274
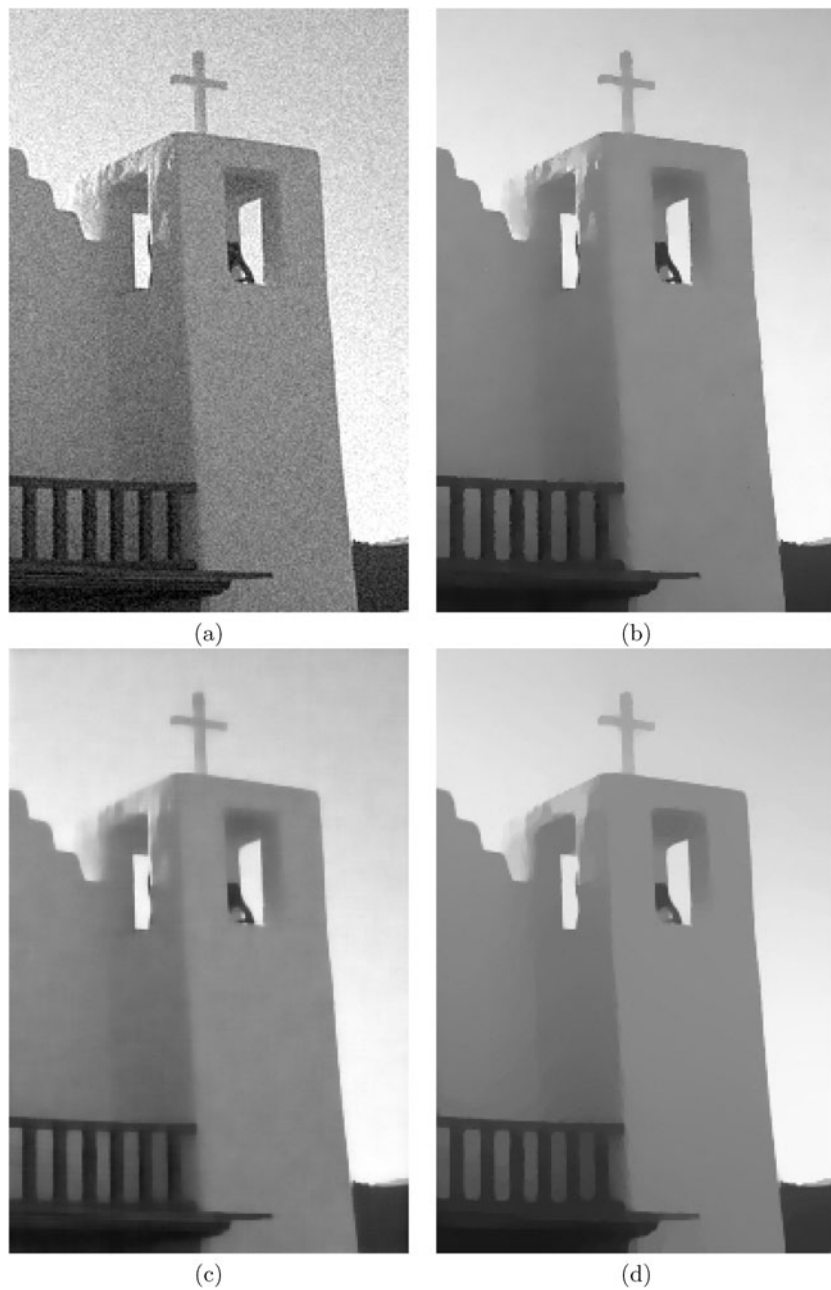
ting the orientation. In Fig. 3, the graph of computed results are presented in order to see visual difference. The result (f) is obtained by (5.1) with $M^4(0.4, 0.1, 10^{-3})$. The denoised image from the proposed method has a clean shape. It preserves sharp edges and smoothly changing pixel values near the edges. We observe that results from other methods do not have very sharp edges except the TV model. The result (e) from the TV denoising model has the stair-case effect on smooth regions. These results are expected in Sect. 2.2.

Example 2

In Fig. 4, we compare results from different methods with larger noise in test 4 in Fig. 2. For a regularization of the

tangent vector field in (c) and (d), $V(5 \cdot 10^{-2}, 1, 10^{-4})$ is used. The result of the proposed method in (c) is obtained by $M^1(10^{-3}, 2, 10^{-3})$. (d), (e), and (f) are obtained by $M^2(10^{-3}, 4, 10^{-4})$, $M^3(80)$, and $M^4(0.5, 1, 10^{-3})$. Now, we observe that the effect of the first step (2.3) to the second step in (2.8), (2.6), and (5.1) is numerically shown. The first row in Fig. 5 is a part of images in Fig. 4. In the second row, we obtain a relatively less smooth vector field with $V(0.1, 3, 10^{-4})$. (b2) is obtained by $M^1(10^{-3}, 2, 10^{-3})$ and we use same parameters for (b1) and (b3) as (a1) and (a3). Note that the result (b2) does not have very clean edge even if we use smaller μ in the second step for the previous model (2.6). The other methods, (2.6) and (5.1), are re-

Fig. 8 (Color online)
Comparison with other methods
in image inpainting: (**a**) is the
original image with the
inpainting domain which is the
red region. (**b1**), (**b2**), (**b3**), and
(**b4**) are the results of the
proposed method (3.14), the
TVS inpainting model (3.12),
the TV inpainting model, and a
fusion model (5.1), respectively.
The *second* and the *fourth rows*
are corresponding graphs of the
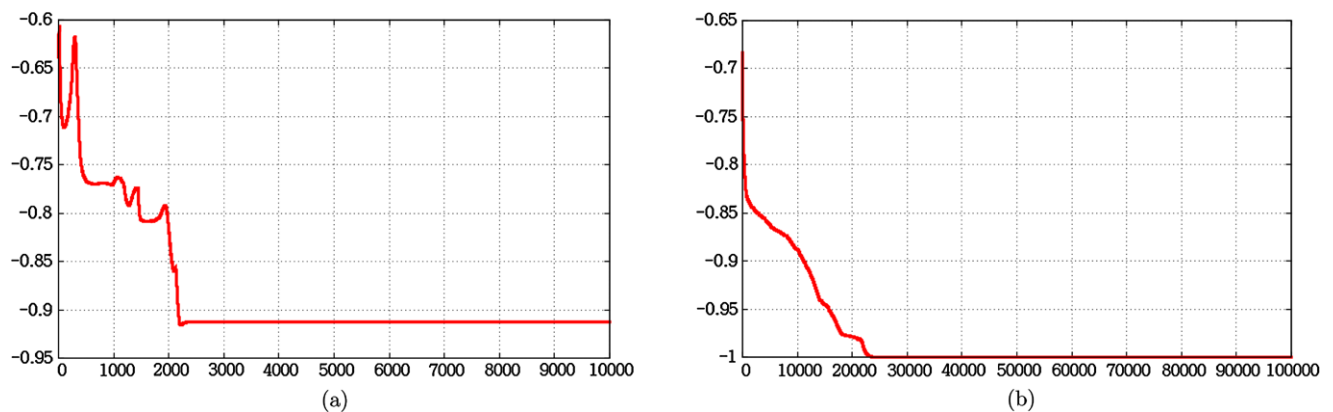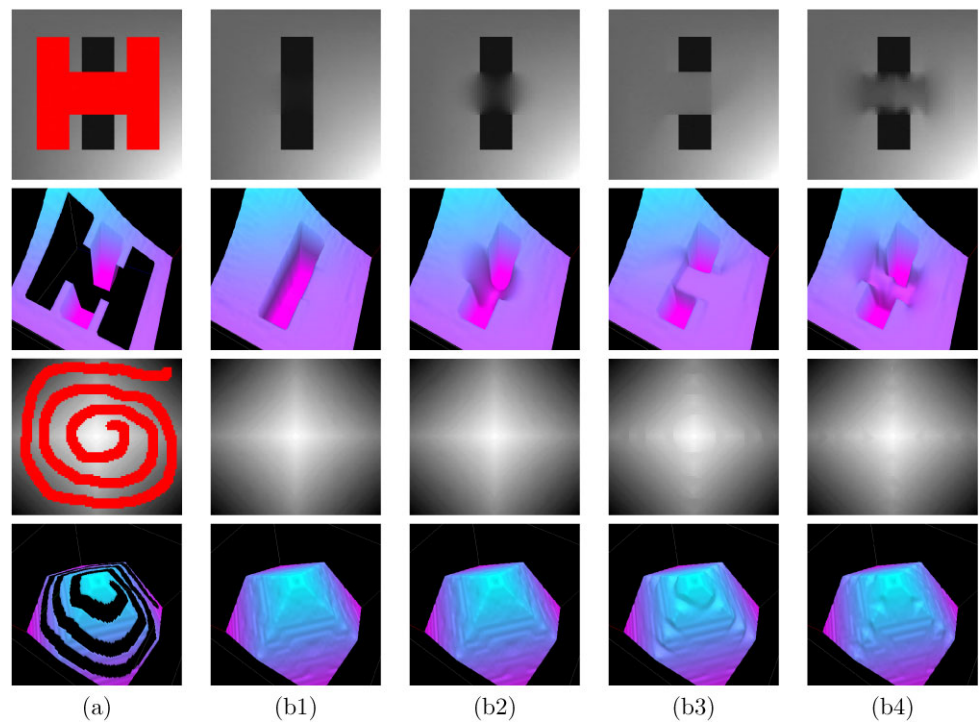*above images*. The inpainting
region in the graph is the hole of
surface

(a)   (b1)   (b2)   (b3)   (b4)

(a)

(b)

Fig. 9 A graph of the energy (3.13): (**a**) and (**b**) are images in the first and the third row at the column (b1) in Fig. 8, respectively

Fig. 10 (Color online) The role
of two positive constants in the
proposed model (3.13): (**a**) is
the original image and the *red
region* in (**b**) is the inpainting
domain. (**c**) and (**d**) are the
results with $\bar{\mu} = 0.001$ and
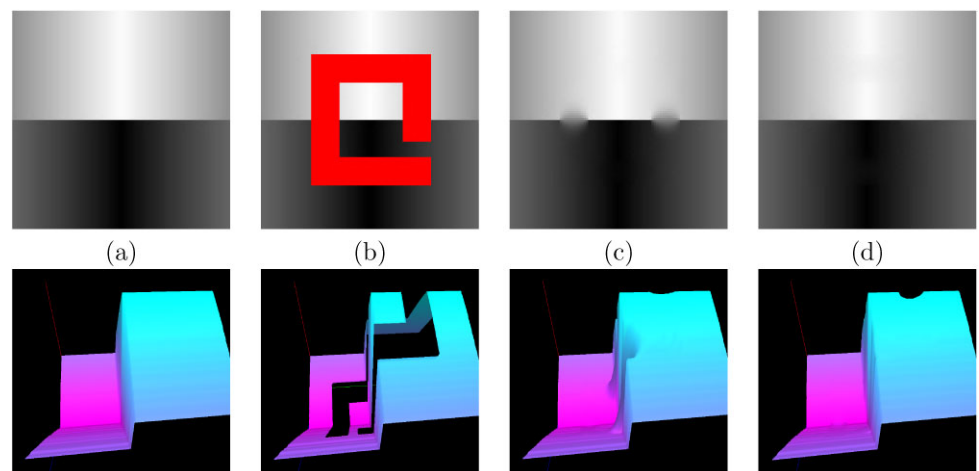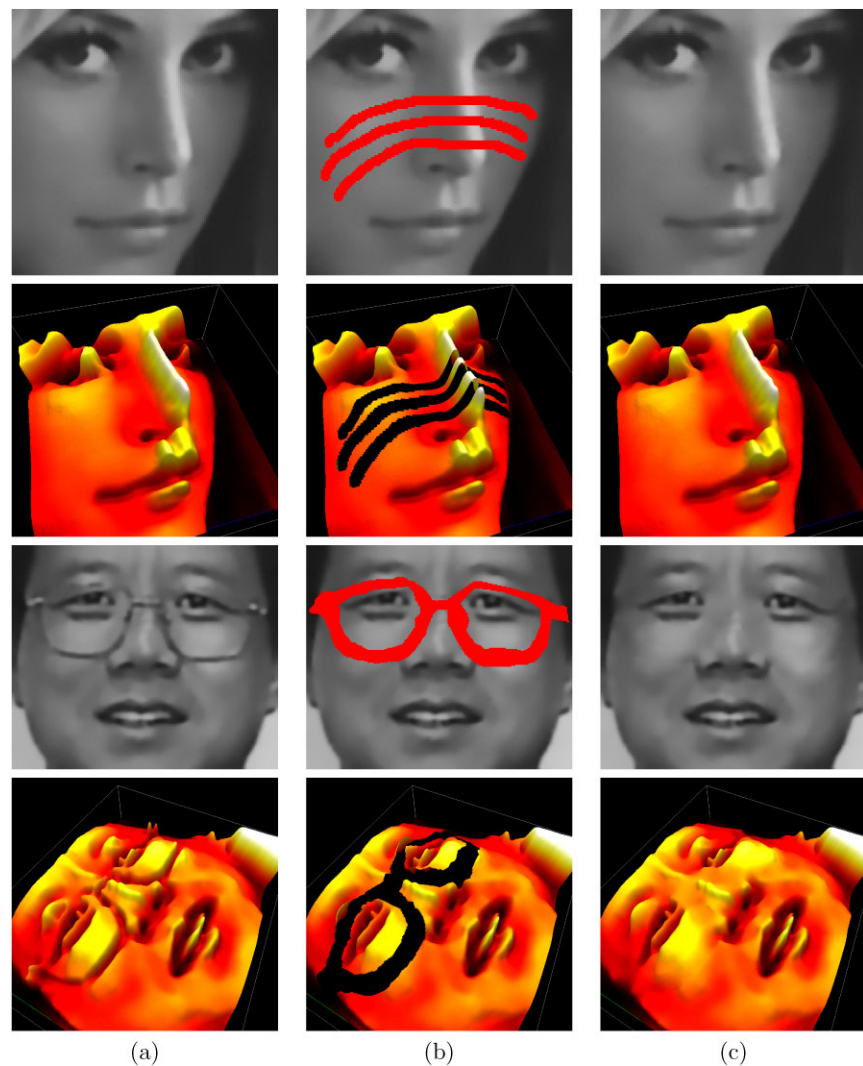$\bar{\mu} = 1$, respectively

(a)   (b)   (c)   (d)

(a)   (b)   (c)

sponded by a small change of the vector field because the field is directly used in the formulation without considering any relation with the image data.
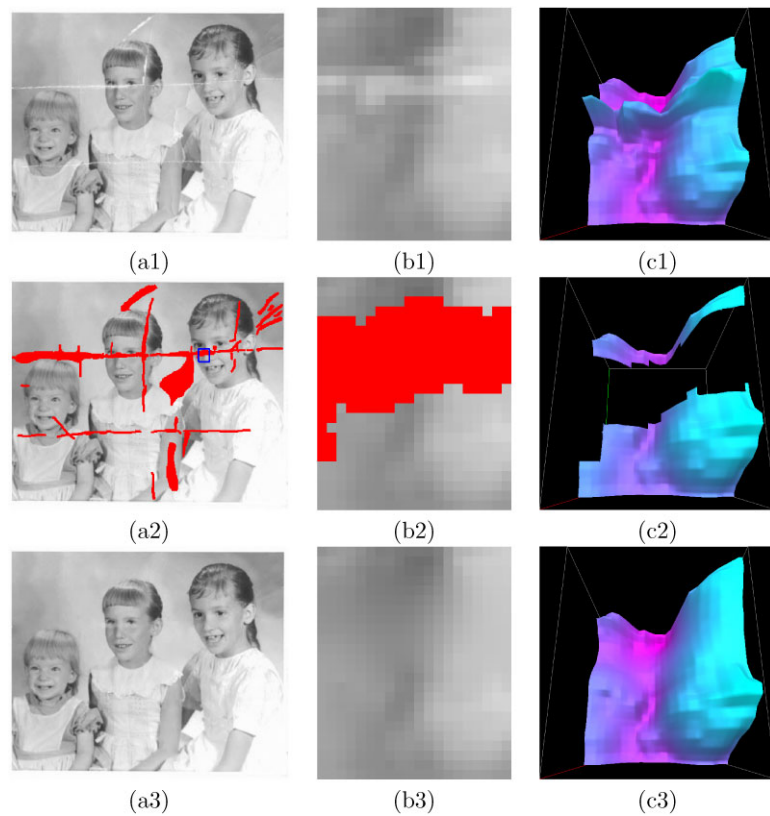
Example 3

For real images, we compare with denoised images from different methods. In Fig. 6, the image (a) is obtained by the proposed method with $V(0.1, 5, 10^{-4})$ and $M^1(5 \cdot 10^{-4}, 5, 5 \cdot 10^{-4})$. (b) is from $V(5 \cdot 10^{-2}, 5, 10^{-4})$ and $M^2(10^{-3}, 1, 5 \cdot 10^{-3})$. (c) is from $M^3(60)$. In Fig. 7, the image (a) is obtained by the proposed method with $V(0.1, 2, 10^{-4})$ and $M^1(10^{-4}, 30, 10^{-3})$. (b) is from $V(0.1, 2, 10^{-4})$ and $M^2(10^{-3}, 2, 10^{-3})$. (c) is from $M^3(60)$. For these images, two models (2.5) and (2.7) give similar results which are better than the TV denoising model.

Example 4

In Fig. 8, we compare with results of image inpainting from different methods. The red regions in (a) are inpainting domains. The first image in the first row has sharp edges and smoothly changing pixel values. The first image in the third row has discontinuities of gradient of the image surface. The regularized vector field in the first and the third row are obtained by $V(10^{-2}, 10^{-3})$. The images (b1), (b2), (b3), and (b4) in first row are obtained by $M^1(10^{-3}, 1, 10^{-3}, 5 \cdot 10^{-2})$, $M^2(10^{-5}, 10^{-6})$, $M^3(10^{-5}, 10^{-6})$, and $M^4(10^{-5}, 1, 5 \cdot 10^{-4})$, respectively. In the same order at the third row, we use $M^1(10^{-4}, 10^{-3}, 10^{-4}, 10^{-2})$, $M^2(10^{-5}, 10^{-6})$, $M^3(10^{-4}, 10^{-5})$, and $M^4(10^{-5}, 1, 10^{-4})$, respectively. The orientation difference γ (5.2) between the normal vectors of the original image and the reconstructed image is measured in Table 3. In order to verify that the proposed energy (3.13) is numerically minimized, we show the graph of the energy in Fig. 9.

Two synthetic examples in Fig. 8 show clear differences between the proposed model and the TV inpainting model. In the first row, the connectivity principle (Chan and Shen 2001) in image inpainting is shown. The height of the inpainting domain in the middle is deliberately chosen to be longer than the width of the black vertical bar in the original image. From the same regularized vector field in the first step, the inpainting results in the first row, (b1) from the proposed model and (b2) from the TVS model, are quite different because the proposed orientation-matching functional has the additional transportation property; see Sect. 3.2. The result from the TV inpainting model is already observed and mathematically analyzed in Chan and Shen (2002). The curvature of the level curve is used in the CCD model and the Euler's elastica model to achieve the long connectivity. The sharp edges and smoothly changing pixels near the edges are well reconstructed in the result image from the proposed model. In the third row, the TV inpainting model has the stair-case effect which the proposed model and the TVS model do not have. Considering the similarity to the fourth-order method (3.8) in the first step, the regularized normal vector field has discontinuities of the normal vector to the level curves of the image. Such discontinuities generate the good reconstruction of the image along the ridges and valleys in the proposed model.

Example 5

In Fig. 10, we discuss the role of parameter $\bar{\mu}$ in (3.13). (a) is the original image and (b) shows the inpainting domain which is the red region. The regularized normal vector is obtained by $V(10^{-2}, 10^{-3})$. In (c) and (d), we only change the parameter $\bar{\mu}$, that is, $M^1(10^{-3}, 10^{-3}, 10^{-3}, 5 \cdot 10^{-3})$ and $M^1(10^{-3}, 1, 10^{-3}, 5 \cdot 10^{-3})$, respectively. As we observed in numerical examples of image denoising, the proposed orientation-matching term captures the sharp edges which are the discontinuities of the image data. So, if we choose a small $\bar{\mu}$, it is difficult to recover sharp edges in (c). If $\bar{\mu}$ is large in (d), those edges are easily recovered. However, it gives a weak force to restore the discontinuities of the gradient of the image data.

Example 6

In Figs. 11 and 12, we show that the proposed inpainting model recovers smooth regions without the stair-case effect for real images. Since we assume that given images are clean, the images in Fig. 11-(a) are preprocessed by the PM denoising method to reduce some noise in the original image. The parameters $V(10^{-2}, 10^{-3})$ are used for the first row in Fig. 11 and Fig. 12. The third row in Fig. 11, we use $V(10^{-4}, 10^{-5})$. In the reconstruction step, $M^1(10^{-4}, 10^{-3}, 10^{-4}, 5 \cdot 10^{-2})$ and $M^1(10^{-4}, 10^{-2}, 10^{-4},$

Table 4 The test image is shown in the test 1 in Fig. 2. The denoised results are obtained by the proposed method (2.7) via the AOS method. The CPU time is measured in second

Size	First step		Second step	
	Total iteration	CPU time	Total iteration	CPU time
32^2	75	3.55	17	0.74
64^2	53	10.56	13	1.18
128^2	60	50.11	12	4.45
256^2	58	221.17	14	21.88
512^2	60	1085.07	19	131.99

$5 \cdot 10^{-2}$) are used for the first row in Fig. 11 and Fig. 12, respectively. $M^1(10^{-5}, 10^{-3}, 10^{-4}, 5 \cdot 10^{-2})$ is used for the third row in Fig. 11. The proposed inpainting model shows good visual quality in surfaces of images.

Example 7

In Table 4, we show the computational speed of the AOS method in image denoising. The simple image, the test 1 in Fig. 2, is used in the different size from 32×32 to 512×512. In the first step, we use $V(0.1, 1, 10^{-4})$. In the second step, $M^1(10^{-3}, 1, 10^{-3})$ is fixed for all images. It seems to follow the second order method. The code is programmed on MATLAB and the Intel Core Duo CPU P8600 2.40 GHz is used. In case of image inpainting, it usually takes more time because the time step is smaller than image denoising case.

6 Conclusions

We proposed an orientation-matching minimization functional for denoising and inpainting digital images. Our algorithm consists of two steps. In the first step, we use the regularized tangent vector field with the incompressibility condition which was suggested in Tai et al. (2006). The condition is crucial for reconstructing an image from the vector field. In the second step, the present work proposed a minimization of an orientation alignment functional between the image gradient and the regularized normal direction. This functional yields a nonlinear PDE for reconstructing images, which exhibits an adaptive diffusivity depending on the orientation of the regularized normal vector field. This allows to obtain images which have sharp edges and smooth regions. We show improved image recovery results in various numerical experiments.

References

Ballester, C., Bertalmio, M., Caselles, V., Sapiro, G., & Verdera, J. (2001). Filling-in by joint interpolation of vector fields and gray levels. *IEEE Transactions on Image Processing*, *10*(8), 1200–1211.

Bertalmio, M. (2006). Strong-continuation contrast-invariant inpainting with a third-order optimal PDE. *IEEE Transactions on Image Processing*, *15*(7), 1934–1938.

Bertalmio, M., Sapiro, G., Caselles, V., & Ballester, C. (2000). Image inpainting. In *Computer graphics SIGGRAPH* (pp. 417–424).

Bertalmio, M., Bertozzi, A. L., & Sapiro, G. (2001). Navier-Stokes, fluid dynamics, and image and video inpainting. In *Proc. conf. comp. vision pattern rec.* (pp. 355–362).

Bresson, X., & Chan, T. F. (2008). Fast dual minimization of the vectorial total variation norm and applications to color image processing. *Inverse Problems and Imaging*, *2*(4), 455–484.

Brox, T., Weickert, J., Burgeth, B., & Mrázek, P. (2006). Nonlinear structure tensors. *Image Vision Computer*, *24*, 41–55.

Catté, F., Lions, P. L., Morel, J.-M., & Coll, T. (1992). Image selective smoothing and edge detection by nonlinear diffusion. *SIAM Journal on Numerical Analysis*, *29*(1), 182–193.

Chan, T. F., & Shen, J. (2001). Nontexture inpainting by curvature driven diffusion (CDD). *Journal of Visual Communication and Image Representation*, *12*, 436–449.

Chan, T. F., & Shen, J. (2002). Mathematical models for local nonexture inpaintings. *SIAM Journal on Applied Mathematics*, *62*(3), 1019–1043.

Chan, T. F., & Shen, J. (2005). Variational image inpainting. *Communications on Pure Applied Mathematics*, *58*, 579–619.

Chan, T., & Vese, L. (2001). Active contours without edges. *IEEE Transactions on Image Processing*, *10*(2), 266–277.

Chan, T. F., Kang, S.-H., & Shen, J. (2002). Euler's elastica and curvature based inpaintings. *SIAM Journal on Applied Mathematics*, *63*(2), 564–594.

Chan, R. H., Setzer, S., & Steidl, G. (2008). Inpainting by flexible Haar-wavelet shrinkage. *SIAM Journal on Imaging. Science*, *1*, 273–293.

Chessel, A., Cao, F., & Fablet, R. (2006). Interpolating orientation fields: An axiomatic approach. In *ECCV06* (pp. IV, pp. 241–254).

Dong, F., Liu, Z., Kong, D., & Liu, K. (2009). An improved LOT model for image restoration. *Journal of Mathematical Imaging and Vision*, *34*, 89–97.

Hahn, J., & Lee, C.-O. (2009). A nonlinear structure tensor with the diffusivity matrix composed of the image gradient. *Journal of Mathematical Imaging and Vision*, *34*, 137–151.

Kimmel, R., & Bruckstein, A. M. (2001). Regularized Laplacian zero crossings as optimal edge integrators. *International Journal of Computer Vision*, *53*, 225–243.

Kornprobst, P., & Aubert, G. (2006). Explicit reconstruction for image inpainting. In *Research report N. 5905 INRIA*.

Lindenbaum, M., Fischer, M., & Bruckstein, A. M. (1994). On Gabor's contribution to image enhancement. *Pattern Recognition*, *27*(1), 1–8.

Litvinov, W. G., Rahman, T., & Tai, X.-C. (2009). *A modified TV-Stokes model for image processing*. Technical report, Preprints—Herausgeber: Institut für Mathematik der Universität Augsburg 2009-25.

Lu, T., Neittaanmaki, P., & Tai, X.-C. (1992). A parallel splitting up method for partial differential equations and its application to Navier-Stokes equations. *RAIRO Mathematical Modeling and Numerecal Analysis*, *26*(6), 673–708.

Lysaker, M., & Tai, X.-C. (2006). Iterative image restoration combining total variation minimization and a second-order functional. *International Journal of Computer Vision*, *66*, 5–18.

Lysaker, M., Lundervold, A., & Tai, X.-C. (2003). Noise removal using fourth-order partial differential equation with applications to medical magnetic resonance images in space and time. *IEEE Transaction on Image Processing*, *12*(12), 1579–1590.

Lysaker, M., Osher, S., & Tai, X.-C. (2004). Noise removal using smoothed normals and surface fitting. *IEEE Transactions on Image Processing*, *13*(10), 1345–1357.

Martin, D., Fowlkes, C., Tal, D., & Malik, J. (2001). A database of human segmented natural images and its application to evaluating segmentation algorithms and measuring ecological statistics. In *Proc. 8th int'l conf. computer vision* (Vol. 2, pp. 416–423), July 2001.

Masnou, S., & Morel, J.-M. (1998). Level lines based disocclusion. In *Proc. IEEE int. conf. on image processing*, Chicago, IL (pp. 259–263).

Perona, P. (1998). Orientation diffusion. *IEEE Transactions on Image Processing*, *7*(3), 457–467.

Perona, P. & Malik, J. (1990). Scale space and edge detection using anisotropic diffusion. *IEEE Transactions on Pattern Analysis and Machine Intelligence*, *12*(7), 629–639.

Rahman, T., Tai, X.-C., & Osher, S. (2007). A TV-Stokes denoising algorithm. In *Scale space and variational methods in computer vision* (pp. 473–482). Heidelberg: Springer.

Rudin, L. I., Osher, S., & Fatemi, E. (1992). Nonlinear total variation based noise removal algorithms. *Physica D*, *60*, 259–268.

Sochen, N. A., Sagiv, C., & Kimmel, R. (2004). Stereographic combing a porcupine or studies on direction diffusion in image processing. *SIAM Journal on Applied Mathematics*, *64*(5), 1477–1508.

Spira, A., Kimmel, R., & Sochen, N. (2007). A short-time Beltrami kernel for smoothing images and manifolds. *IEEE Transactions on Image Processing*, *16*, 1628–1636.

Steidl, G., & Teuber, T. (2009). Anisotropic smoothing using double orientations. In *SSVM '09: proceedings of the second international conference on scale space and variational methods in computer vision* (pp. 477–489). Berlin: Springer.

Tai, X.-C., Osher, S., & Holm, R. (2006). Image inpainting using TV-Stokes equation. In *Image processing based on partial differential equations* (pp. 3–22). Heidelberg: Springer.

Tang, B., Sapiro, G., & Caselles, V. (2000). Diffusion of general data on non-flat manifolds via harmonic maps theory: The direction diffusion case. *International Journal of Computer Vision*, *36*, 149–161.

Terzopoulos, D. (1988). The computation of visible-surface representations. *IEEE Transactions on Pattern Analysis and Machine Intelligence*, *10*(4), 417–438.

Tschumperlé, D., & Deriche, R. (2002). Orthonormal vector sets regularization with PDE's and applications. *International Journal of Computer Vision*, *50*(3), 237–252.

Vese, L. A., & Osher, S. (2002). Numerical methods for p-harmonic flows and applications to image processing. *SIAM Journal on Numerical Analysis*, *40*(6), 2085–2104.

Weickert, J. (1999). Coherence-enhancing diffusion filtering. *International Journal of Computer Vision*, *31*, 111–127.

Weickert, J., & Welk, M. (2006). Tensor field interpolation with PDEs. In Weickert, J., & Hagen, H. (Eds.) *Visualization and processing of tensor fields* (pp. 315–325). Berlin: Springer.

Weickert, J., ter Harr Romeny, B. M., & Viergever, M. A. (2001). Efficient and reliable schemes for nonlinear diffusion filtering. *IEEE Transactions on Image Processing*, *7*, 398–410.